

# Electro-optofluidics: achieving dynamic control on-chip

Mohammad Soltani,<sup>1,2,3</sup> James T. Inman,<sup>1</sup> Michal Lipson,<sup>3,4</sup> and Michelle D. Wang<sup>1,2,\*</sup>

<sup>1</sup>Laboratory of Atomic and Solid State Physics, Department of Physics, Cornell University, Ithaca, New York 14853, USA

<sup>2</sup>Howard Hughes Medical Institute, Cornell University, Ithaca, New York 14853, USA

<sup>3</sup>Department of Electrical and Computer Engineering, Cornell University, Ithaca, New York 14853, USA

<sup>4</sup>Kavli Institute at Cornell University, Ithaca, New York 14853, USA

\*[mdw17@cornell.edu](mailto:mdw17@cornell.edu)

**Abstract:** A vital element in integrated optofluidics is dynamic tuning and precise control of photonic devices, especially when employing electronic techniques which are challenging to utilize in an aqueous environment. We overcome this challenge by introducing a new platform in which the photonic device is controlled using electro-optical phase tuning. The phase tuning is generated by the thermo-optic effect using an on-chip electric microheater located outside the fluidic channel, and is transmitted to the optofluidic device through optical waveguides. The microheater is compact, high-speed ( $> 18$  kHz), and consumes low power ( $\sim$ mW). We demonstrate dynamic optical trapping control of nanoparticles by an optofluidic resonator. This novel electro-optofluidic platform allows the realization of high throughput optofluidic devices with switching, tuning, and reconfiguration capability, and promises new directions in optofluidics.

© 2012 Optical Society of America

OCIS codes: (130.3120) Integrated optics devices; (230.5750) Resonators.

---

## References and links

1. D. Psaltis, S. R. Quake, and C. Yang, "Developing optofluidic technology through the fusion of microfluidics and optics," *Nature* **442**(7101), 381–386 (2006).
2. C. Monat, P. Domachuk, and B. J. Eggleton, "Integrated optofluidics: a new river of light," *Nat. Photonics* **1**(2), 106–114 (2007).
3. X. D. Fan and I. M. White, "Optofluidic microsystems for chemical and biological analysis," *Nat. Photonics* **5**(10), 591–597 (2011).
4. H. Schmidt and A. R. Hawkins, "Photonics integration of non-solid media using optofluidics," *Nat. Photonics* **5**(10), 598–604 (2011).
5. A. M. Armani, R. P. Kulkarni, S. E. Fraser, R. C. Flagan, and K. J. Vahala, "Label-free, single-molecule detection with optical microcavities," *Science* **317**(5839), 783–787 (2007).
6. A. H. J. Yang, S. D. Moore, B. S. Schmidt, M. Klug, M. Lipson, and D. Erickson, "Optical manipulation of nanoparticles and biomolecules in sub-wavelength slot waveguides," *Nature* **457**(7225), 71–75 (2009).
7. X. Serey, S. Mandal, Y. F. Chen, and D. Erickson, "DNA transport and delivery in thermal gradients near optofluidic resonators," *Phys. Rev. Lett.* **108**(4), 048102 (2012).
8. S. Y. Lin, E. Schonbrun, and K. Crozier, "Optical manipulation with planar silicon microring resonators," *Nano Lett.* **10**(7), 2408–2411 (2010).
9. U. Levy and R. Shamai, "Tunable optofluidic devices," *Microfluid Nanofluid* **4**(1-2), 97–105 (2008).
10. S. K. Y. Tang, B. T. Mayers, D. V. Vezenov, and G. M. Whitesides, "Optical waveguiding using thermal gradients across homogenous liquids in microfluidic channel," *Appl. Phys. Lett.* **88**(6), 061112 (2006).
11. A. J. Chung and D. Erickson, "Optofluidic waveguides for reconfigurable photonic systems," *Opt. Express* **19**(9), 8602–8609 (2011).
12. L. Diehl, B. G. Lee, P. Behroozi, M. Loncar, M. A. Belkin, F. Capasso, T. Aellen, D. Hofstetter, M. Beck, and J. Faist, "Microfluidic tuning of distributed feedback quantum cascade lasers," *Opt. Express* **14**(24), 11660–11667 (2006).
13. A. Groisman, S. Zamek, K. Campbell, L. Pang, U. Levy, and Y. Fainman, "Optofluidic 1x4 switch," *Opt. Express* **16**(18), 13499–13508 (2008).
14. D. Erickson, T. Rockwood, T. Emery, A. Scherer, and D. Psaltis, "Nanofluidic tuning of photonic crystal circuits," *Opt. Lett.* **31**(1), 59–61 (2006).

15. R. Shamaï and U. Levy, "On chip tunable micro ring resonator actuated by electrowetting," *Opt. Express* **17**(2), 1116–1125 (2009).
16. L. J. Zhou and A. W. Poon, "Electrically reconfigurable silicon microring resonator-based filter with waveguide-coupled feedback," *Opt. Express* **15**(15), 9194–9204 (2007).
17. C. Manolatou, M. J. Khan, S. H. Fan, P. R. Villeneuve, H. A. Haus, and J. D. Joannopoulos, "Coupling of modes analysis of resonant channel add-drop filters," *IEEE J. Quantum Electron.* **35**(9), 1322–1331 (1999).
18. B. S. Schmidt, A. H. J. Yang, D. Erickson, and M. Lipson, "Optofluidic trapping and transport on solid core waveguides within a microfluidic device," *Opt. Express* **15**(22), 14322–14334 (2007).
19. V. R. Almeida, R. R. Panepucci, and M. Lipson, "Nanotaper for compact mode conversion," *Opt. Lett.* **28**(15), 1302–1304 (2003).
20. A. H. Atabaki, E. Shah Hosseini, A. A. Eftekhar, S. Yegnanarayanan, and A. Adibi, "Optimization of metallic microheaters for high-speed reconfigurable silicon photonics," *Opt. Express* **18**(17), 18312–18323 (2010).
21. N. Sherwood-Droz, H. Wang, L. Chen, B. G. Lee, A. Biberman, K. Bergman, and M. Lipson, "Optical 4x4 hitless silicon router for optical networks-on-chip (NoC)," *Opt. Express* **16**(20), 15915–15922 (2008).
22. P. Dong, W. Qian, H. Liang, R. Shafiqi, D. Feng, G. Li, J. E. Cunningham, A. V. Krishnamoorthy, and M. Asghari, "Thermally tunable silicon racetrack resonators with ultralow tuning power," *Opt. Express* **18**(19), 20298–20304 (2010).
23. R. R. Brau, P. B. Tarsa, J. M. Ferrer, P. Lee, and M. J. Lang, "Interlaced optical force-fluorescence measurements for single molecule biophysics," *Biophys. J.* **91**(3), 1069–1077 (2006).
24. Q. F. Xu, B. Schmidt, S. Pradhan, and M. Lipson, "Micrometre-scale silicon electro-optic modulator," *Nature* **435**(7040), 325–327 (2005).
25. A. Pertsinidis, Y. Zhang, and S. Chu, "Subnanometre single-molecule localization, registration and distance measurements," *Nature* **466**(7306), 647–651 (2010).
26. B. Sun, D. S. Johnson, G. Patel, B. Y. Smith, M. Pandey, S. S. Patel, and M. D. Wang, "ATP-induced helicase slippage reveals highly coordinated subunits," *Nature* **478**(7367), 132–135 (2011).
27. A. L. Forget and S. C. Kowalczykowski, "Single-molecule imaging of DNA pairing by RecA reveals a three-dimensional homology search," *Nature* **482**(7385), 423–427 (2012).
28. A. L. Robinson, "New ways to make microcircuits smaller," *Science* **208**(4447), 1019–1022 (1980).
29. J. Happel and H. Brenner, *Low Reynolds number hydrodynamics: with special applications to particulate media* (Noordhoff International Publishing, Leiden, 1973).
30. M. Soltani, Q. Li, S. Yegnanarayanan, and A. Adibi, "Improvement of thermal properties of ultra-high Q silicon microdisk resonators," *Opt. Express* **15**(25), 17305–17312 (2007).

## 1. Introduction

Integrated optofluidics holds abundant promise for biological and chemical research by miniaturizing complex optical and fluidic functionalities to the micro/nanoscale [1–8]. This emerging technology enables high throughput study and analysis of chemical and biological molecules through their detection and manipulation on-chip. Despite major progress in this field, a missing element is the lack of active tunability and reconfigurability of the optical devices, especially using electronic techniques. In a prospective optofluidic chip with hundreds of optical devices, the on-chip laser source is preferred to be fixed and, therefore, all other optical devices need to be tuned relative to the laser wavelength. This requires the realization of compact and power efficient tuning mechanisms. Prior work in tuning optofluidic devices [9] has primarily focused on modifying the refractive index of the fluid, either by changing the fluid, or modifying other physical properties to change the fluid properties [9–15]. Such tuning mechanisms are, by nature, either slow and consume high power, or are too large to integrate into nanophotonic chips. Therefore, alternative tuning mechanisms are required to directly change the optical properties of the device, rather than changing the properties of the surrounding fluid. This is especially important in biological experiments wherein the aqueous buffer cannot be changed.

Here we propose and demonstrate a platform for tunable integrated optofluidic devices that are sensitive to a phase change remotely induced by the thermo-optic effect. In our approach, the phase information is sent via an optical waveguide to the optofluidic device. The phase tuning device can be realized by integrating an on-chip electric microheater, outside the fluidic channel, to transfer thermal energy locally and efficiently to the waveguide. Because most fluids are electrolytes, co-localization of electronics and photonics in fluid could result in the corrosion of the electronics and unwanted conduction of electric current through the fluid. This design alleviates the need for co-localization in an aqueous solution. It

also eliminates heat transfer through the fluid and undesirable temperature changes in the fluid.

## 2. Electro-optofluidic device design

Figure 1(a) shows an example of the integration of a microheater with an optofluidic resonator for tuning its optical responses. The device consists of an optical traveling-wave resonator coupled to two waveguides that are themselves connected at their ends to form an external feedback path for the resonator. This type of resonator architecture, containing a feedback loop, has been used in a different context for electro-optic modulators [16]. In our design, the resonator resides in a fluidic channel, whereas the optical feedback loop responsible for induced phase changes in the resonator is located outside the fluidic channel and is covered by a dielectric material with a refractive index smaller than that of the waveguides. A metal microheater is placed a few microns above the feedback arm to minimize optical loss from the waveguide, due to the presence of metal, but still permit efficient heat transfer to the arm. The microheater is composed of a metal heating element and low resistivity metal contact electrodes for applying electric current to the heater.

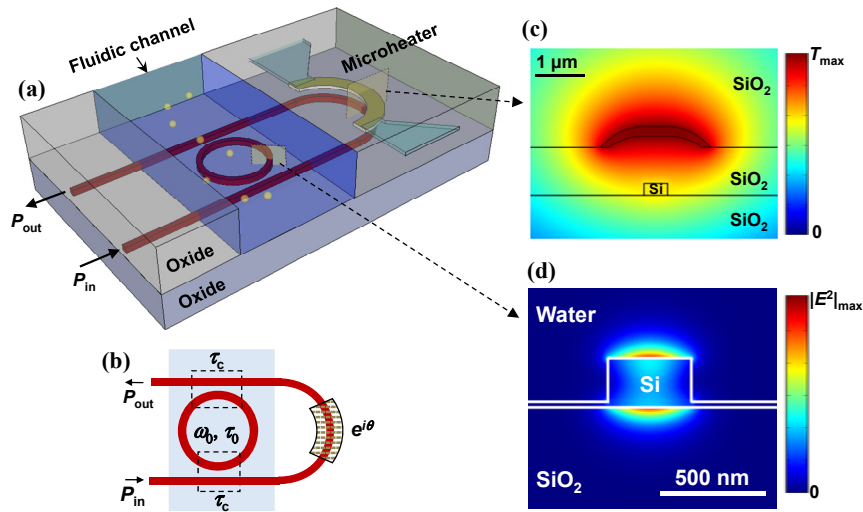


Fig. 1. Design architecture for the integration of an electric microheater into an optofluidic resonator. (a) A schematic of a device. In this device, a traveling-wave resonator (such as a microring, microdisk, or racetrack) resides within a fluidic channel and is side-coupled to two waveguides that are themselves connected to form a feedback loop for the resonator. The feedback loop is extended outside the fluidic channel and is buried in an oxide layer for interfacing with a metal heater. The heater is located above the feedback arm and isolated from the fluid (electrically) and the waveguide (optically) via oxide layers. The two ends of the heater are connected to metal electrodes. The oxide cladding transfers heat from the metal heater to the waveguide. The cladding over the heater is also oxide. The yellow spheres in the fluidic channel indicate nanoparticles. (b) A simplified two-dimensional schematic of the device presented in (a) with general design parameters indicated. (c) Calculated temperature distribution of the microheater (nickel) with a Si waveguide underneath. The calculations are for a cross-section of the device as indicated in (a). A bending in the heater has been considered for the heater geometry because of the morphology of the underlying oxide layer deposited on top of the waveguide. These parameters were chosen to closely match those in fabricated devices. The waveguide is implemented on silicon-on-insulator (SOI) with a silicon device thickness of 250 nm and a buried oxide (BOX) thickness of 3  $\mu\text{m}$ . In all the simulations, the cross-section of the waveguides is 440 nm (width) and 250 nm (height), and the cross-section of the heater is 2.5  $\mu\text{m}$  (width) and 200 nm (height). (d) Calculated distribution of the squared magnitude of the electric field ( $|E|^2$ ) for the fundamental TM mode of a silicon resonator for the cross section as indicated in (a). A nanoparticle would be trapped on top of the resonator where the field strength is maximal.

In order to understand the operation principles of the device, we can analyze it using temporal coupled-mode theory (CMT) [17] (see Appendix A1 for details). Figure 1(b) shows a simplified two dimensional schematic of the device with its detailed parameters. From CMT analysis, we find that the net resonance frequency of the device is:  $\omega'_0 = \omega_0 - 2 \sin(\theta + \theta_0) / \tau_c$  and the net coupling lifetime of the resonator to the waveguide is:  $\tau'_c = \tau_c / [2(1 + \cos(\theta + \theta_0))]$ . In these expressions,  $\omega_0$  is the intrinsic resonance frequency of the resonator,  $\tau_c$  is the intrinsic coupling lifetime between the resonator and each waveguide,  $\theta_0$  is the phase shift due to the length of the feedback arm, and  $\theta$  is the phase change due to the microheater. Hence, the resonance frequency of the resonator can be tuned by changing the phase in the feedback arm. Also, through modifying  $\tau_c$  by phase change, the extinction of the transmission spectrum and its linewidth can both be further tuned. As a result, the frequency, the linewidth, and the extinction ratio of the resonance can be modified by changing the phase in the feedback arm.

We implemented the device shown in Fig. 1(a) in a silicon-on-insulator (SOI) platform, as Si has both a large thermo-optic coefficient ( $1.86 \times 10^{-4} \text{ K}^{-1}$ ) and a large refractive index (3.475). We also designed the device to operate at a wavelength near 1550 nm because many commercially available tunable lasers and optical equipment work in this range. Figure 1(c) shows the calculated steady-state temperature distribution for a cross-section of the metal heater with a waveguide located underneath. As shown, the temperature at the silicon waveguide is ~65% of the maximum temperature occurring at the center of the heater. This high temperature efficiency is due to the close proximity of the waveguide to the heater. In addition, the temperature increase is localized within a few microns of the microheater: the temperature change required to shift the resonance, by an amount corresponding to its linewidth, is a few degrees at the feedback arm, while there is essentially no temperature increase at the resonator due to the microheater.

In the design and experiments presented here, we used transverse magnetic (TM) polarization (electric field predominantly normal to the wafer plane) for the waveguides and resonators. Figure 1(d) shows the calculated distribution of the squared magnitude of the electric field for TM polarization at a cross section of the silicon resonator that is seated on a SiO<sub>2</sub> substrate with water cladding. As seen from this distribution, this polarization has a stronger field along the top surface of the resonator as compared with that along the side surfaces. This makes TM polarization more suitable for sensing and optical trapping applications, as opposed to the alternative transverse electric (TE) polarization (electric field predominantly in the wafer plane) [18] [see also Appendix A2].

### 3. Device fabrication

Figure 2 is an optical microscope image of a fabricated device. The resonator in this device is a racetrack resonator and is located within the fluidic channel. The extended length of the feedback arm allows for an increased overlap with the heater, resulting in a larger phase shift. The fabrication process of the device began with patterning the waveguides and resonators using electron-beam lithography. maN 2403 was used as a resist mask followed by plasma etching, with an etch depth of ~225 nm and leaving an ~25 nm silicon spacer layer. This spacer layer was meant for the post CMOS wet etching processes, wherein buffered hydrofluoric acid (BHF) was used and the presence of the thin Si spacer protects the underneath oxide layer from being attacked by the BHF. The waveguide and resonators were clad with a 1  $\mu\text{m}$  plasma-enhanced chemical vapor deposition (PECVD) oxide. The process was continued with two subsequent steps of lithography, metal evaporation, and lift-off to define the metal heater (Ni) and the Al contact electrodes. The Ni heater was 2.5  $\mu\text{m}$  wide and 200 nm thick (10 nm of Titanium was evaporated *a priori* as an adhesion layer between the Ni and the oxide). The Al electrodes had a thickness of 700 nm. The metal heater and electrodes were covered by another 1.5  $\mu\text{m}$  of oxide to isolate them from the fluid. Hence, the overall oxide thickness above the waveguide was 2.5  $\mu\text{m}$ . This thickness guaranteed an efficient coupling of light from the off-chip light source (using a taper lens fiber) to the input

waveguide (which is initially tapered inversely [19]). In the next step, optical lithography and wet etching using BHF removed the oxide cladding from the waveguides and the resonators and exposed them to the fluid. A subsequent step of optical lithography and plasma etching removed the oxide from a portion of the Al contact electrodes and exposed them to the off-chip metal probes.

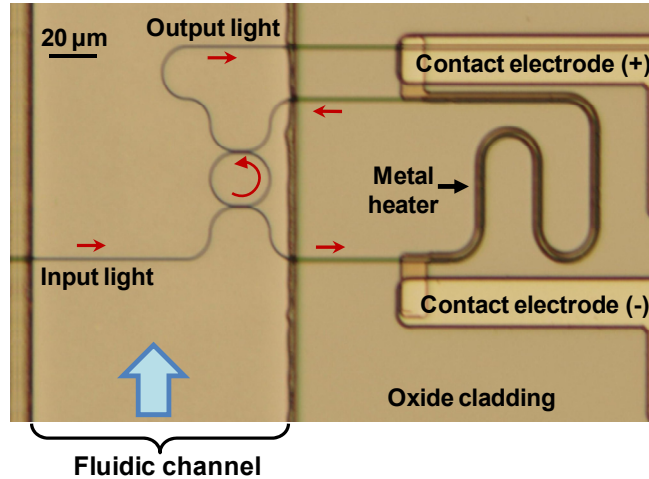


Fig. 2. An optical microscope image of a fabricated optofluidic resonator integrated with a microheater. Note that the resonator is within the fluidic channel, whereas the microheater is located outside. The resonator is a 'racetrack' with a bend radius of  $10\ \mu\text{m}$  and a straight length of  $5\ \mu\text{m}$ .

The next step was to integrate the chip with a microfluidic channel. In conventional microfluidic fabrication, PDMS is used as the channel seal and is bonded to the top surface of the fabricated chip. However, PDMS distorts the image when the fluidic device is imaged through a microscope. Therefore, in this work, a glass film ( $170\ \mu\text{m}$  thickness) was bonded to the chip to form the fluidic channel seal. For simplicity of fabrication, the glass was bonded to the device surface using Parafilm and the fluidic channel boundaries were defined by a Parafilm layer, both from the sides as well as by the chip and glass surfaces from bottom and top, respectively. In a more advanced construction, the glass can be bonded to the device top surface using wafer bonding techniques in microfabrication technology. The flow inlet and outlet holes can be perforated into the glass or the device substrate. For this device, we etched the holes through the device substrate (silicon) and fluid was flowed in and out from the back of the substrate.

#### 4. Device characterization

We have achieved tunability of the optofluidic resonator using the integrated microheater. The spectrum of the resonator was characterized by scanning the wavelength of the laser coupled to the chip (see Appendix A3 for the details of characterization). To tune the resonance spectrum, a voltage was applied to the microheater using a microprobe. Figure 3(a) shows the measured spectrum of one of the resonances of the device at three different voltages. The full-width half-maximum (FWHM) linewidth of the measured resonance is  $\sim 0.22\ \text{nm}$  and a clear resonance spectrum shift was observed after a voltage was applied to the device. The application of  $1.4\ \text{V}$  to the microheater shifted the resonance by an amount equal to the FWHM of the resonator. The consumed electric power for this shift was  $\sim 8\ \text{mW}$ . By further optimization of the microheater geometry and additional refinement of the fabrication techniques, this power consumption can be further reduced to the sub-mW range [20–22]. Figure 3(b) compares the theoretical prediction (see Appendix A4) and experimental data for

resonance shift versus the voltage applied to the microheater. There is a close correspondence between the prediction and experimental data.

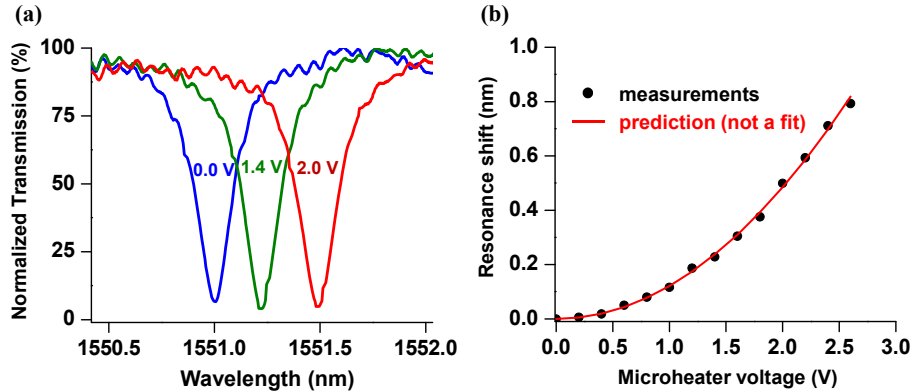


Fig. 3. Experimental demonstration of electrical tuning of the optofluidic resonator shown in Fig. 2. (a) Resonator tuning by the microheater. The resonator spectrum was measured via the transmission of the waveguide as different voltages were applied to the microheater. The input power to the waveguide was in the sub-mW range. (b) Resonance wavelength dependence on the applied voltage to the microheater. Solid dots are measurements and the solid line is a prediction based on theoretical calculations.

To realize a high throughput optofluidic chip, fast tuning of optical devices is essential. As shown in Fig. 4, a square-wave voltage was applied to the microheater and the transmission response of the resonator was measured. The measured rise time is  $\sim 8.5 \mu\text{s}$  and the fall time is  $\sim 55 \mu\text{s}$ . This demonstrates that the microheater can operate at frequencies  $> 18 \text{ kHz}$ , making the tuning mechanism many times to orders of magnitude faster than other tuning methods [13–15]. The response time, as well as the power consumption of the heater, can be further reduced by optimizing the parameters of the microheater [20–22].

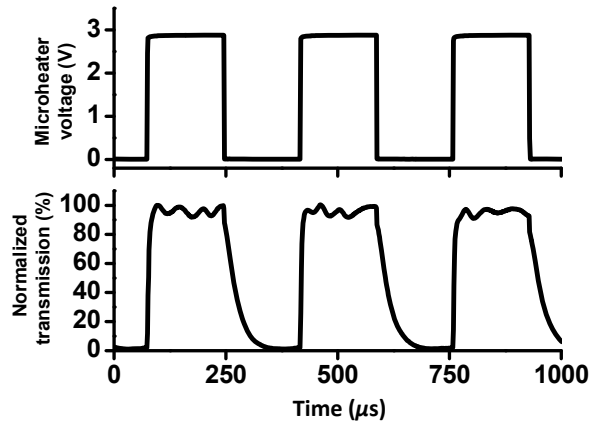


Fig. 4. Determination of the response time of the resonator to the microheater. The response of the resonator was measured via the transmission of the waveguide as a square-wave voltage, at a frequency of 3 kHz, was applied to the microheater.

Finally, we have also demonstrated dynamic control of optical trapping of a nanoparticle by the optofluidic resonator (Fig. 5). For this experiment, the laser wavelength was fixed at the resonance of the resonator when the microheater was off, and polystyrene nanoparticles, 790 nm in diameter, were injected into the fluidic channel. Once a single nanoparticle was trapped by the resonator, it circulated around the resonator in the direction of laser power

circulation. By applying a high frequency square wave (indicated by a yellow square-wave symbol) to the microheater, the resonator was tuned to the input laser frequency for only a fraction of time (see Appendix A5 for details of the experiment) and as a result, the nanoparticle speed was decreased. The frequency of the square-wave was high enough that the nanoparticle could not escape the resonator. This switching method offers a solution to minimize photobleaching in experiments that require concurrent trapping and fluorescence, by interlacing the trapping laser with a fluorescence excitation laser [23].

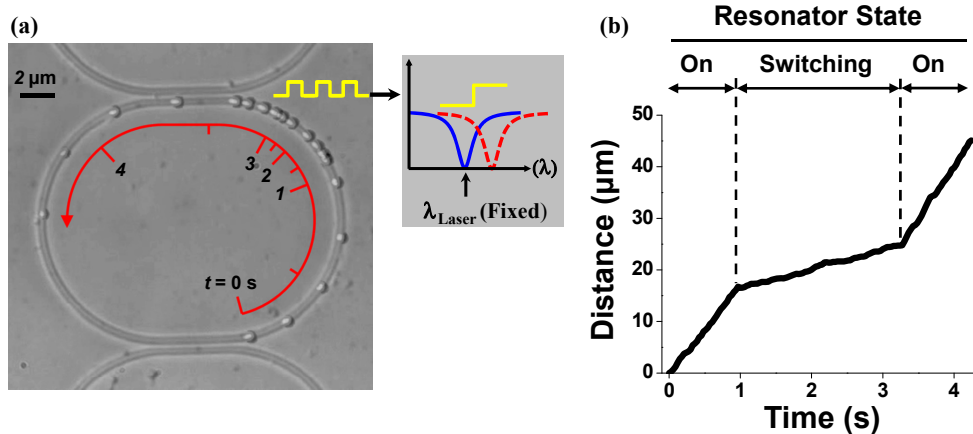


Fig. 5. Demonstration of nanoparticle trapping control using the electrically tunable resonator. (a) The trajectory of a single nanoparticle, optically trapped by the resonator, is presented in overlaid progressive images, taken at 0.24 s time intervals. The particle circulated on the resonator in the direction of light propagation. For  $t = 0$  to 1.2 s, no voltage was applied to the microheater and the resonator was on resonance. For  $t = 1.2$  to 3.3 s, a 10 kHz square-wave voltage was applied to the microheater so that the resonator was periodically tuned on- and off-resonance. The subfigure (to the right) shows the resonance shift when voltage was applied. A video of the trapping experiment is available online ([Media 1](#)). (b) The corresponding distance versus time for the particle measured by image tracking shown in (a).

## 5. Discussion

Although in this work we used the thermo-optic effect, other physical effects, such as the electro-optic effect in silicon that induce a phase change in the waveguides could, in principle, also be used to change the refractive index. This would require the integration of a P-i-N diode with the waveguide to induce the refractive index shift [24]. The refractive index change due to the electro-optic effect in silicon is weaker than the thermo-optic effect. However, the response time of the electro-optic effect in silicon is much faster than that of the thermo-optic effect [24]. Since most dynamic phenomena are slow in fluids, a thermo-optic based device would be suitable for most applications. While waveguides may be fabricated from a variety of optical materials that have thermo-optic effects, we focused on materials which were compatible with mass manufacturing micro- and nano- fabrication technologies, such as complementary-metal-oxide-semiconductor (CMOS) technology. For this purpose, silicon (Si), silicon nitride ( $\text{Si}_3\text{N}_4$ ), and silicon dioxide ( $\text{SiO}_2$ ) are widely used in CMOS technology and were natural candidates. Si is optically transparent in the wavelength range of 1200 nm and above;  $\text{Si}_3\text{N}_4$  is transparent in a much broader wavelength range spanning the entire visible range to infrared (IR) and mid IR;  $\text{SiO}_2$  can be used as the cladding layer as it has a lower refractive index than those of Si and  $\text{Si}_3\text{N}_4$ .

## 6. Conclusions

We have presented a novel device design and fabrication techniques to electrically control an optofluidic device. We demonstrate that by using compact microheaters, the resonance of an

optofluidic resonator can be tuned locally, rapidly, and with low power consumption. Such an electro-optofluidic device, and its active feedback controllability, has many applications including sensing, trapping, switching, adaptive calibration, and particle monitoring. While the focus of this paper was specifically on electric tunability of an optical resonator inside a fluid, our device and method could be extended to a variety of waveguide and resonator based nanophotonic functionalities in an optofluidic platform. This electro-optofluidic integration with active tuning/switching capability holds promise for detection and manipulation of single molecules in biology (for examples, ref [25–27]) in a high throughput manner. In addition, it opens new avenues to the realization of very-large-scale-integration (VLSI) optofluidics analogous to VLSI electronic circuits [28].

## Appendices

### *A1. Details of the principle operation of the optofluidic resonator with a feedback arm*

In this section, we show the details of the CMT analysis of the device. Figure 6(a) shows the schematic of the waveguide-resonator device with the detailed parameters indicated. As seen from this figure, amplitudes of  $S_{\text{in}}$ ,  $S_1$ ,  $S_2$ , and  $S_{\text{out}}$  have been designated for the waveguide mode at each port of the waveguide to the resonator. These amplitudes are normalized such that their squared magnitudes determine the waveguide mode power. Also, an amplitude of  $a$  is assigned to the resonator, and it is normalized such that its squared magnitude determines the resonator energy. Using CMT, the device in Fig. 6(a) can be analyzed as follows:

$$\begin{aligned} \frac{da}{dt} &= (i\omega_0 - \frac{1}{\tau_0} - \frac{1}{\tau_c} - \frac{1}{\tau'_c})a + kS_{\text{in}} + kS_2, \\ S_1 &= S_{\text{in}} - k^*a, \\ S_2 &= S_1 e^{i\theta'}, \quad (\theta' = \theta + \theta_0), \\ S_{\text{out}} &= S_2 - k^*a, \end{aligned} \quad (1)$$

where  $k$  is the coupling constant between the waveguide and the resonator and is related to the coupling lifetime  $\tau_c$  as  $|k|^2 = 2/\tau_c$ . By Fourier transforming the above equations and combining them, the following expression can be obtained:

$$\frac{P_{\text{out}}}{P_{\text{in}}} = \left| \frac{i(\omega - \omega'_0) + 1/\tau_0 - 1/\tau'_c}{i(\omega - \omega'_0) + 1/\tau_0 + 1/\tau'_c} e^{i\theta'} \right|^2, \quad (2)$$

where  $\tau'_c$  and  $\omega'_0$  are as defined in the main text. From the above expression, we see that the net resonance frequency of the device is  $\omega'_0$ . The total lifetime of the resonator  $\tau$  is given by:

$$\frac{1}{\tau} = \frac{1}{\tau_0} + \frac{1}{\tau'_c}. \quad (3)$$

In addition, critical coupling (i.e., zero transmission) occurs at the resonance frequency  $\omega'_0$  if:

$$\tau_0 = \tau'_c = \tau_c / [2(1 + \cos \theta')]. \quad (4)$$

From these expressions, we see that we can adjust the transmission extinction and resonance linewidth by adjusting the phase of the phase shifter.

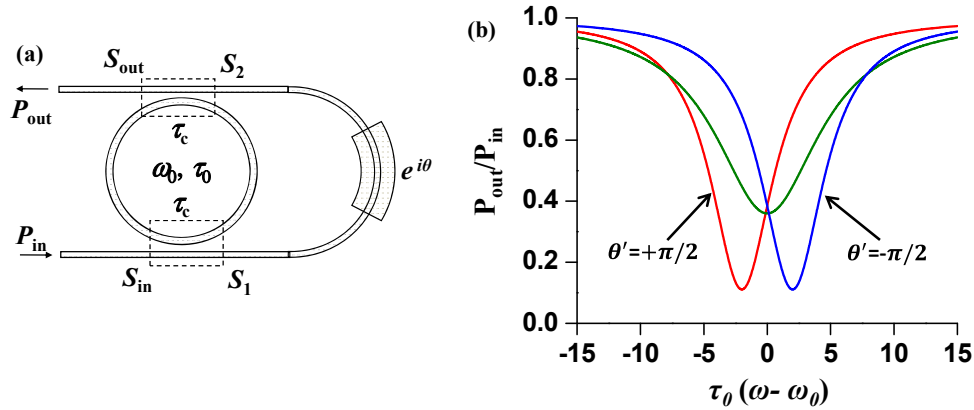


Fig. 6. (a) A ring resonator side-coupled to two waveguides, which are themselves connected at one end. A tunable phase shifter has been added to the connection arm. (b) Transmission spectrum of the device in (a) for three values of  $\theta' = +\pi/2$  (red), 0 (green),  $-\pi/2$  (blue), respectively. In (b) we have assumed  $\tau_0 = \tau_c$ .

Figure 6(b) shows the theoretically predicted power transmission spectrum for three values of phase of the feedback arm, as indicated. From this figure, resonance shift, extinction variation, and linewidth changes are clearly observed by modifying the phase of the feedback arm.

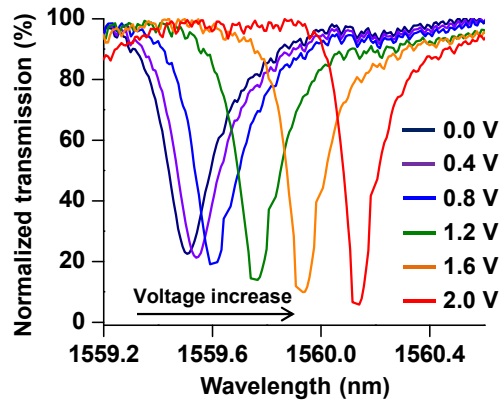


Fig. 7. Experimental results on the variation of the optofluidic resonator spectrum when different voltages are applied to the microheater (from 0 V to 2 V with steps of 0.4 V).

Figure 7 shows experimental results on the spectral modification induced in the optofluidic resonator when voltage was applied to the microheater. As the voltage was increased, we observed shifted resonance, narrowed linewidth, and an increase in the extinction. We emphasize that by biasing the phase shift to some values and locally modifying the phase around this bias point, the change in the extinction and the linewidth can be minimized (see Fig. 3(a)). The bias point can be designed statically by adjusting the length of the feedback arm, or dynamically by applying the voltage to the microheater.

#### A2. TM vs. TE polarization for optical trapping

When a dielectric nanoparticle or biomolecule (typically non-magnetic) is trapped by the evanescent tail of an optical waveguide or resonator mode, the strength of the trapping is proportional to the energy stored in the particle, as well as the decay length of the evanescent field. The stored energy, to the first order approximation, is proportional to the squared magnitude of the electric field of the waveguide or resonator. Figure 8 shows the calculated

distribution of  $|E|^2$  for both TM and TE polarizations, respectively. As seen from this figure, the TM mode has more of its field distribution outside and on the top surface of the waveguide. In contrast, the TE mode has most of its field distribution residing inside the waveguide, along with some outside the vertical sidewalls. For the waveguide dimensions considered in this manuscript, the calculations show that the evanescent decay lengths of  $|E|^2$  for both modes are within the same range (50 nm for TE and 70 nm for TM) in the vertical direction on the top surface of the waveguide. Therefore, overall, the TM polarization is more suitable for trapping. Trapping will take place above the top surface of the waveguide, which has a larger surface area to capture nanoparticles.

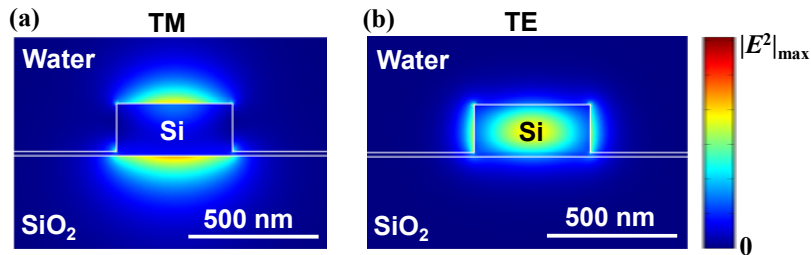


Fig. 8. Calculated distribution of the squared magnitude of the electric field ( $|E|^2$ ) on a cross section of a silicon waveguide. (a) The TM mode (electric field is predominantly normal to the plane of the chip). (b) The TE mode (electric field is predominantly parallel to the plane of the chip). The waveguide dimensions are the same as defined in the main text.

#### A3. Detailed experimental and characterization methods

For the experiment, tunable laser light (at 1550 nm) was coupled to the chip using an optical tapered lensed fiber. A polarization controller adjusted the light polarization for maximum coupling of light from the fiber to the TM polarization mode of the waveguide. The transmitted light through the chip was collected from the opposite end of the chip using an additional tapered lens optical fiber and ultimately sent to a photodetector. Using syringe pumps, aqueous solution was flowed into the fluidic channel through inlet/outlet holes located at both ends of the channel. A microprobe, for applying electric voltage, was connected to the contact electrodes of the microheater. By sweeping the laser wavelength and monitoring the transmitted power through the chip using the photodetector, the spectrum of the resonator was characterized. The spectrum characterization was performed as different voltages were applied to the microheater. The measured resistance of the heater and the electrodes is  $\sim 120 \Omega$ . Considering the dimensions of the heater and the electrodes, the estimated resistance value for the heater is  $\sim 60 \Omega$ , and  $\sim 60 \Omega$  for the electrodes. To measure the microheater response time, the laser wavelength was fixed near the resonance, and a square wave voltage, with a frequency of 3 kHz and duty cycle of 50%, was applied to the microheater. Using a photodetector with a bandwidth of 50 MHz, the transmission of the resonator through the waveguide was measured and, from that, the response time of the microheater was obtained.

#### A4. Calculation of resonance shift versus the microheater voltage and comparison with experiment

The heat power generated by the microheater is:  $P = V^2/R$ , where  $V$  is the voltage applied to the heater and  $R$  is the heater resistance. The temperature rise in the waveguide, due this heat, is:  $\Delta T = P/K$ , where  $K$  is the effective thermal conductance. Combining the above two expressions we have:  $\Delta T = V^2/(KR)$ . Also, from the thermo-optic effect, the resonance wavelength shift is related to the temperature change as:  $\Delta \lambda = A_T \Delta T$ , where  $A_T$  is the effective thermo-optic resonance shift coefficient. By combining the last two expressions we have:

$$\Delta\lambda = A_T \frac{V^2}{KR} . \quad (5)$$

The above equation shows the quadratic variation of the resonance wavelength versus the applied voltage. The parameters in Eq. (5) can be obtained as follows. From the Heat equation and the simulated structure shown in Fig. 1(b), the effective thermal conductance of the heater was obtained to be  $1.94 \times 10^{-3} \text{ WT}^{-1}$ . Also, knowing that the resonance shift of the resonator is  $\Delta\omega = 2 \sin(\theta')/\tau_c$ , we can approximate it as  $\Delta\omega = 2 \theta'/\tau_c$  when  $\theta'$  is near zero or a multiple integer factor of  $\pi$ . Using the relation  $\Delta\omega/\omega_0 = -\Delta\lambda/\lambda_0$  we can find the variation of the resonance wavelength as

$$\Delta\lambda = \frac{2\theta' \lambda_0}{\tau_c \omega_0} = \frac{\theta' \lambda_0}{Q_c} \quad (6)$$

where  $Q_c = \omega_0\tau_c/2$  is the coupling quality factor between the resonator and the waveguide. Also, variation of  $\theta'$  due to the change in the refractive index of the waveguide because of the temperature change is obtained as  $\theta' = 2\pi L\Delta n_{\text{eff}}/\lambda_0$ , in which  $L$  is the length of the heater on the waveguide ( $174 \mu\text{m}$  in this work) and  $\Delta n_{\text{eff}}$  is the change in the effective index of the mode of the waveguide due to the temperature. Because, most of the mode energy density (not to be confused with  $|E|^2$ ) is concentrated in the core of the silicon waveguide and the thermo-optic coefficient of silicon ( $\alpha_T = dn/dT = 1.86 \times 10^{-4} \text{ T}^{-1}$ ) is much stronger than that of the surrounding oxide, then with a very good approximation we can say  $\Delta n_{\text{eff}} = \alpha_T \Delta T$ . As a result, we have  $\theta' = 2\pi L \alpha_T \Delta T / \lambda_0$ . By putting this expression in Eq. (6), we obtain:

$$\Delta\lambda = \frac{2\pi\alpha_T\Delta T}{Q_c} = \frac{2\pi\alpha_T L}{Q_c} \frac{V^2}{KR} \quad (7)$$

In our waveguide-resonator design the value of  $Q_c$  was 12000. By putting the values for  $K$  ( $1.94 \times 10^{-3} \text{ WT}^{-1}$ ),  $R$  ( $120 \Omega$ ),  $L$  ( $274 \mu\text{m}$ ), and  $\alpha_T$  ( $1.86 \times 10^{-4} \text{ T}^{-1}$ ) in Eq. (7), the theoretical curve for the resonance wavelength shift versus the applied voltage can be obtained which is in a very good agreement with the experimental results.

#### *A5. Details of the dynamic optical trapping experiment*

For the optical trapping experiment, polystyrene nanoparticles, 790 nm in diameter, were injected into the microfluidic channel. The laser power was increased to increase the trapping energy above the thermal Brownian noise. When the laser wavelength was tuned on the resonance wavelength, the particles were trapped by the resonator and circulated around it. From Fig. 4(b) in the text, the measured speed of the nanoparticle was  $\sim 17 \mu\text{m/s}$ . Given that this particle traveled near the resonator surface we can estimate the drag force on it using Faxen's law [18, 29]. Figure 9 shows the calculated force for different spacing between the nanoparticle and the surface. Assuming 10 nm spacing between the nanoparticle and the waveguide surface, the drag force is  $\sim 0.3 \text{ pN}$ . This force should be equal to the optical scattering force resulting in the nanoparticle moving with a constant speed. From an electromagnetic simulation and calculating optical scattering force on the nanoparticle using Maxwell's stress tensor, the amount of circulated power in the resonator that results in this force value can be obtained as  $\sim 12 \text{ mW}$ .

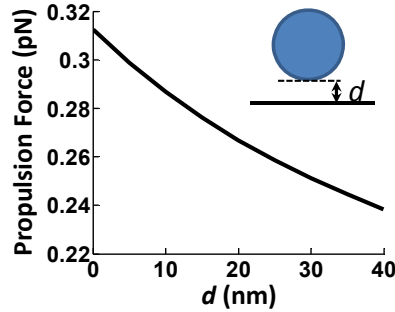


Fig. 9. Calculated drag force on a 790 nm polystyrene nanoparticle moving with a speed of  $\sim 17 \mu\text{m/s}$  at different distances above a surface. The inset shows the nanoparticle and its distance from the resonator top surface.

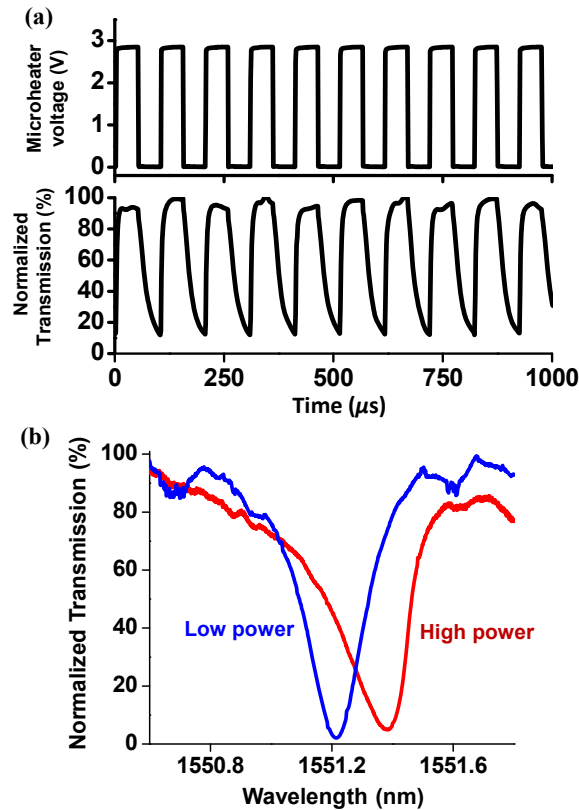


Fig. 10. (a) The applied square-wave voltage to the microheater at 10 kHz and the response of the resonator by measuring its transmission through the waveguide for data shown in Fig. 4. (b) Measured spectrum of the resonator at low ( $\sim$ sub-milli Watt) and high ( $\sim 6\text{-}8 \text{ mW}$ ) input optical power.

During the trapping experiment, by applying a square-wave voltage to the microheater, the resonator was switched on and off periodically. This could control the circulation power in the resonator and consequently the speed of the nanoparticle. For the square-wave voltage, we applied different frequencies in the range of 1 kHz to 10 kHz, and in all the cases the nanoparticle did not escape the optical trap of the resonator. For the trapping experiment discussed in the main text, the frequency of the square-wave voltage was 10 kHz with a 50% duty cycle. Figure 10 (a) shows this voltage and the response of the resonator. As seen from

this figure, during the half-cycle that the microheater voltage was stepped to zero, the transmitted power did not immediately reach minimum. As a result, the optical power in the resonator did not instantly reach maximum before the microheater voltage was stepped to high. This is the main reason that the speed of the nanoparticle (as determined from the slope of the particle distance versus time plot in Fig. 5(b)) was less than half of the speed when the resonator was always on resonance. However, other physical effects, such as the nonlinearity response of the resonator, could have also affected the dynamics of the nanoparticle. Figure 10(b) shows the spectrum of the resonator at both low and high powers. The asymmetry and broadening observed in the resonance spectrum at high optical powers is due to the nonlinearity effect induced by two-photon absorption and self-heating due to absorption of optical power in the resonator [30].

### **Acknowledgments**

We thank Dr. S. Fellman, Dr. R.M. Fulbright, and other members of the Wang Lab for critical comments on the manuscript. We also thank Drs. B.Y. Smith, M.A. Hall, S. Forth, A. Turner, and A. Nitkowski for helpful discussions. We wish to acknowledge postdoctoral support to M.S. from the Howard Hughes Medical Institute, graduate traineeship support to J.T.I. from Cornell's Molecular Biophysics Training Grant (T32GM008267), support to M.D.W. from National Institutes of Health grant (GM059849) and National Science Foundation grant (MCB-0820293), and support to M.L. from Cornell's Center for Nanoscale Systems funded by the National Science Foundation. This work was performed in part at the Cornell NanoScale Facility, a member of the National Nanotechnology Infrastructure Network, which is supported by its users and the National Science Foundation (Grant ECS-0335765).